3D Printed Wicks for Loop Heat Pipes

Rohit Gupta[1], Chien-Hua Chen[2], and William G. Anderson[3]
Advanced Cooling Technologies, Inc., Lancaster, PA 17601

This paper describes the development of 3D printed wicks for loop heat pipes. This work is part of an overall effort by Advanced Cooling Technologies, Inc. to develop 3D printed loop heat pipes as a low-cost, rapidly-manufacturable alternative technology to standard loop heat pipes for future high-performance small spacecraft. The wicks were built using laser powder bed fusion of standard 316L SS powder. The build parameters were varied by controlling a custom variable called the energy density to produce an assortment of wicks with different capillary metrics, i.e., porosity, permeability, and maximum pore radius. The variation in the capillary metrics, determined using a combination of capillary flow porometry and mercury intrusion porosimetry, was studied with respect to the energy density. The pore distribution was also studied by analyzing in detail the intrusion curves acquired during mercury intrusion porosimetry. The results from this study can serve as general guidelines for building future 3D printed wicks for loop heat pipes with the desired capillary performance.

Nomenclature

D_c	=	characteristic diameter (in μm)
D_{max}	=	pore diameter at maximum hydraulic conductance (in μm)
d	=	point distance (in mm)
E_ρ	=	energy density (in J/mm^3)
h	=	hatch spacing (in mm)
l	=	layer thickness (in mm)
P	=	laser power (in W)
r	=	pore radius (in μm)
r_{eq}	=	maximum equivalent pore radius (in μm)
S	=	volume fraction of pores larger than L_{max}
t	=	exposure time (in s)
φ	=	porosity

I. Introduction

ADVANCED Cooling Technologies, Inc. (ACT) has been working on the development of 3D Printed Loop Heat Pipes (3DP-LHP) as part of several NASA SBIR programs. The 3DP-LHP is a low-cost, rapidly-manufacturable alternative technology to standard Loop Heat Pipe (LHP), exploiting additive manufacturing to eliminate the high-risk, labor-intensive processes that contribute to the high cost and long lead time of a standard LHP. For instance, a standard LHP evaporator fabrication involves several time-consuming steps, such as the primary wick fabrication, wick insertion, knife-edge sealing, etc, which contribute to about 75% of the total cost of an LHP. With 3D printing, the evaporator can be built as a single, continuous unit with all the required subcomponents. This enables complete automation of the evaporator fabrication, leading to over an order-of-magnitude savings in cost. The 3DP-LHP can enable large spacecraft missions within small spacecraft budget and launch cycles with tremendous potential defense and commercial impact. The performance of current small spacecraft is mainly limited by the low heat rejection capability of current low-cost LHP alternatives, such as thermal straps. Since the 3DP-LHP retains the advantage of smooth-walled tubing of an LHP, it can significantly enhance the heat rejection capability through integration with a deployable radiator. The flexibility afforded by 3D printing can also simplify the design cycles of small spacecraft. As a defense application example, a large collection of high-performance small satellites (SmallSats) enabled by 3DP-

[1] R&D Engineer II, 1046 New Holland Avenue, Lancaster, PA 17601.
[2] R&D Manager, 1046 New Holland Avenue, Lancaster, PA 17601.
[3] Chief Engineer, 1046 New Holland Avenue, Lancaster, PA 17601.

LHP can be used to replace existing large communication satellites to reduce susceptibility for robust information sharing. In the commercial domain, 3DP-LHP can enable high-performance SmallSats for sensing, communications, and scientific research. Beyond earth-based applications, this technology can be vital to future Lunar and Martian spacecraft that are expected to be equipped with advanced, high-power scientific instruments.

The overall development and prototype testing of the 3DP-LHP has been described in previous publications of the current authors.[1,2] This paper details the development of the 3DP-LHP wick, a critical LHP component that is primarily employed to provide capillary pumping for loop operation. Additionally, a secondary wick provides capillary pumping for fluid exchange between the evaporator and the compensation chamber. Section II describes the build parameter metric that was controlled to produce an assortment of 3D printed wicks. It also details the measurement techniques employed to ascertain the capillary performance of the wicks. The results of these measurements and their associated implications are discussed in Section III.

II. Methods

In this study, the wick samples were built using laser powder bed fusion of standard spherical 316L SS powder. The sample geometry, CAD rendering, and a photograph is presented in Figure 1, showing a cylindrical porous region, which serves as the wick, and a solid annular wall, which acts as the surrounding envelope. This design was selected to serve as a suitable representation of the 3D printed evaporator, consisting of a primary wick region and a solid envelope. The wick samples were built in the orientation shown in Figure 1 b) and c). The design of the sample featured a conical exclusion from the bottom of the porous region, which allowed the porous region to be offset from the build plate. This offset was introduced deliberately to prevent contamination of the pores during the removal of the sample from the build plate. The bulk dimensions of the wick sample were selected with the goal building the largest possible sample that could be fit inside a standard mercury penetrometer for the purposes of conducting Mercury Intrusion Porosimetry (MIP).

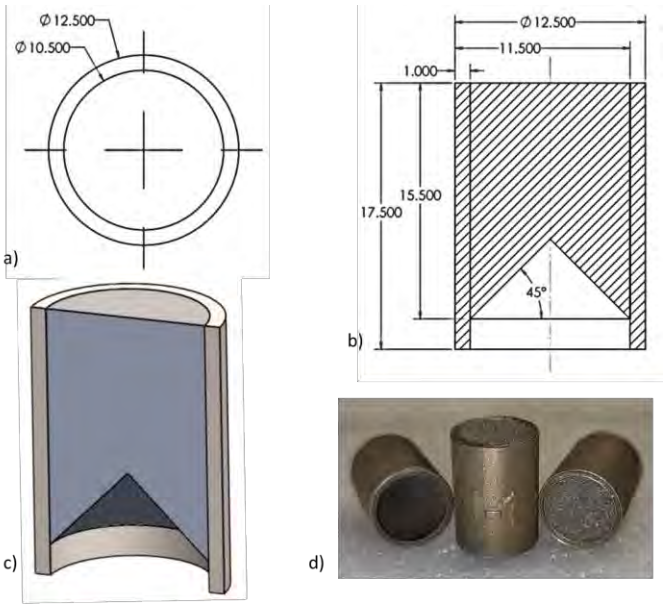

Figure 1. a) Plan and b) elevation drawings of the 3D printed wick sample, c) a vertically-sectioned CAD rendering of the wick sample, and d) a photograph of the wick samples.

In order to introduce finite porosity in the wick region, the input energy associated with the build process was lowered to various pre-determined values. The lowering of the input energy leads to incomplete melting or fusion of the powder, which prevents a complete collapse of the total gap between individual powder particles. Similar strategy for porous builds has been employed by Adnen et al.[3] and Gotoh et al.[4] Similar to Gotoh et al.[4], the build parameters in the current study are also combined into a single parameter called the energy density, E_ρ, that can be intuitively understood as the energy input during a build process. This parameter has units of Joules per cubic millimeter (J/mm^3) and is defined in Equation 1.

$$E_\rho = \frac{P\,t}{h\,d\,l} \tag{1}$$

where P is the laser power in Watts (W), t is the exposure time in seconds (s), h, d, and l are the hatch spacing, point distance, and layer thickness, respectively, in millimeter (mm). A scan of the energy density was conducted in the current study producing a variety of wick samples, which are presented in Section III.

The capillary metrics of the wick samples were determined using a combination of capillary flow porometry and MIP. The capillary flow porometry consisted of a bubble-point test to determine the maximum pore radius and a dry gas flow test to determine the wick permeability. The maximum pore radius sets the capillary limit of the LHP by virtue of the maximum pressure difference across the liquid-vapor interface that can be sustained by the wick, thereby limiting the total pressure drop in the system. The permeability quantifies the ease of flow through the wick and is proportional to the volume flow rate per unit pressure drop in the wick. A high-permeability wick, therefore, allows a higher flow rate for a given pressure drop than a low-permeability wick. In the bubble-point test, the wick sample was first saturated with liquid by submerging it into a bath of Iso-Propyl Alcohol (IPA). The conical end of the sample was then connected to a compressed nitrogen source while the flat end was left submerged in the IPA bath immediately below the level of the liquid, as shown in the schematic presented in Figure 2. Using a pressure regulator, the applied pressure on the conical end was gradually increased until the emergence of the first continuous stream of bubbles from the flat end of the sample, which signaled the breach of the bubble-point pressure. The pressure reading at bubble point, which sets the capillary limit of the LHP, was then used in conjunction with Washburn's equation to determine the maximum equivalent pore radius, r_{eq}, for an equivalent circular pore.

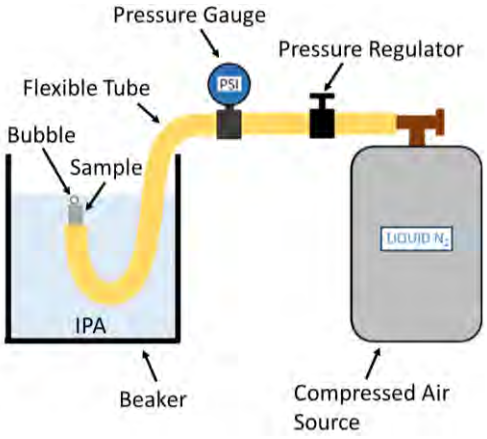

Figure 2. A schematic of the bubble-point test setup.

The IPA bath was removed for the dry gas flow test exposing the sample free end to ambient conditions. A mass flow meter was also installed after the pressure gauge. The volume flow rate of nitrogen at standard atmospheric conditions was then recorded for a range of input pressures. The wick permeability was determined from the acquired measurements using a modified version of Darcy's law to account for the non-traditional sample geometry used in the current study. It should be noted that capillary flow porometry measurements were also conducted with the sample in the opposite orientation, i.e., with the flat surface connected to the compressed nitrogen source, but no discernable difference was noticed within the resolution of the acquired measurements.

MIP on the wick samples was performed by the Materials Characterization Laboratory at The Pennsylvania State University using a Micrometrics Autopore V series mercury porosimeter. MIP was conducted to determine the connected porosity and better understand the morphology of the pores in the sample. The readers should note that the connected pores here refer to those that are accessible from the surface of the sample. The connected porosity therefore includes both the through pores and the dead-end pores, i.e., pores that terminate within the sample. The different effect of these two categories of pores on the capillary performance will be highlighted in Section III. In addition to the dry gas flow test described earlier, the wick permeabilities were also determined from MIP using a well-established form of the Katz-Thompson (K-T) permeability relationship presented in Equation 2. This equation relates the permeability of a porous region to the diameter and volume fraction of pores that are estimated to have the highest hydraulic conductance. A detailed explanation of the mathematical underpinnings of the K-T relationship can be found in their seminal papers.[5,6]

$$\text{Permeability} = \frac{1}{89}(D_{max})^2 \left(\frac{D_{max}}{D_c}\right) \varphi\, S(D_{max}) \left(9.869233 \times 10^{-13}\right) \quad (2)$$

where the permeability is in squared meters (m^2), D_{max} is the pore diameter in micrometer (μm) at maximum hydraulic conductance, D_c is the characteristic diameter in micrometer (μm), which is determined from the threshold pressure at which mercury first spans the sample, φ is the total porosity, and $S(D_{max})$ is the volume fraction of pores with diameter D_{max} and larger.

It should be mentioned that both the maximum equivalent pore radius, r_{eq}, and the pore diameter at maximum hydraulic conductance, D_{max}, provide measures for cross sections of connected paths in the wick. However, these quantities correspond to two different cross sections. For the maximum equivalent pore radius, a throat is defined to aid the discussion. The throat of a path corresponds to the narrowest region or the point of minimum cross section of that path. The maximum equivalent pore radius is the radius of the largest throat of all the connected paths in the wick. This association follows logically from the definition of bubble point. In order for bubbles to emerge from a path, the highest capillary locking for that path, which occurs at the throat, must be breached. Moreover, the first stream of bubbles is expected from the path with the largest throat radius as that will be breached before other paths in the wick. In contrast, the pore diameter at maximum hydraulic conductance is the cross-sectional diameter at the mercury front during the maximum hydraulic conductance event in MIP. In general, the mercury front is not expected to be at the throat of a connected path during maximum hydraulic conductance. As such, the cross section associated with D_{max} is different from the cross section at the throat that is associated with r_{eq}.

III. Results

The results from this study are presented in two separate sub-sections: A. Capillary Flow Porometry and B. Mercury Intrusion Porometry.

A. Capillary Flow Porometry

The capillary metrics of the successfully developed 3D printed wicks are presented in Figure 3 as a function of the build energy density, defined in Equation 1. Any significant reduction in the energy density below the lowest value in Figure 3 was found to lead to build failures due to incomplete consolidation of the metal powder. Energy densities beyond the maximum presented value were not tried due to the low connected porosity of the samples, which would have rendered them unsuitable for LHP applications. Figure 3 a) shows a significant non-linear drop in connected porosity with increasing energy density from over 40% down to under 9% beyond E_ρ = 5 J/mm^3. The drop in porosity is expected as the higher energy density leads to greater melting leaving behind fewer inter-particle gaps. The blue-dashed line represents a least-squares power fit through the data points. The total porosity of the samples is expected to be significantly greater than the connected porosity due to the presence of isolated pores. Gotoh et al.,[4] found that the isolated porosities of their 3D printed 316L SS wicks were broadly contained within 4% and 10% despite large differences in the total porosity. While not useful to the wick permeability, the isolated pores still contribute to reducing the overall thermal conductivity of the wick, which is a favored characteristic for LHP applications as it minimizes heat leak to the evaporator core. Furthermore, the 316L SS material used for the 3D printed wicks has a thermal conductivity of ~16 W/mK, which is approximately six times lower than the thermal conductivity of Nickel, used commonly as the standard wick material in LHPs. Thus, even at the lower porosities, the 3D printed SS wicks can still be expected to have comparable or lower thermal conductivity than the Nickel wicks.

In general correlation with the porosity, the permeability in Figure 3 b) also shows a significant non-linear variation, with a high initial rate of decline that reduces substantially at the higher energy densities. Due to the linear scale used on the permeability axis, the higher energy density samples appear compressed near the zero-permeability line. However, the permeability at the highest energy density is still greater than 10^{-15} m^2 as will be more evident later. Figure 3 c) shows the variation in the maximum equivalent pore radius, which unlike the porosity and permeability, shows a distinct linear dependance on the energy density. A particular highlight is the wick with a pore radius of under 2 μm, which could be developed in the current program. Collectively, the results from Figure 3 can serve as a general guideline for building wicks with the desired capillary metrics. Low-energy-density wicks are preferred for low-power LHP applications wherein the capillary limit can be traded for better thermal conductance from reduced heat leak of high porosity wicks. Similarly, a low energy density wick can also be used as a secondary wick for fluid exchange between the evaporator and the compensation chamber. Moreover, the energy density can be varied during the build process to produce graded wicks with the desired composite properties.

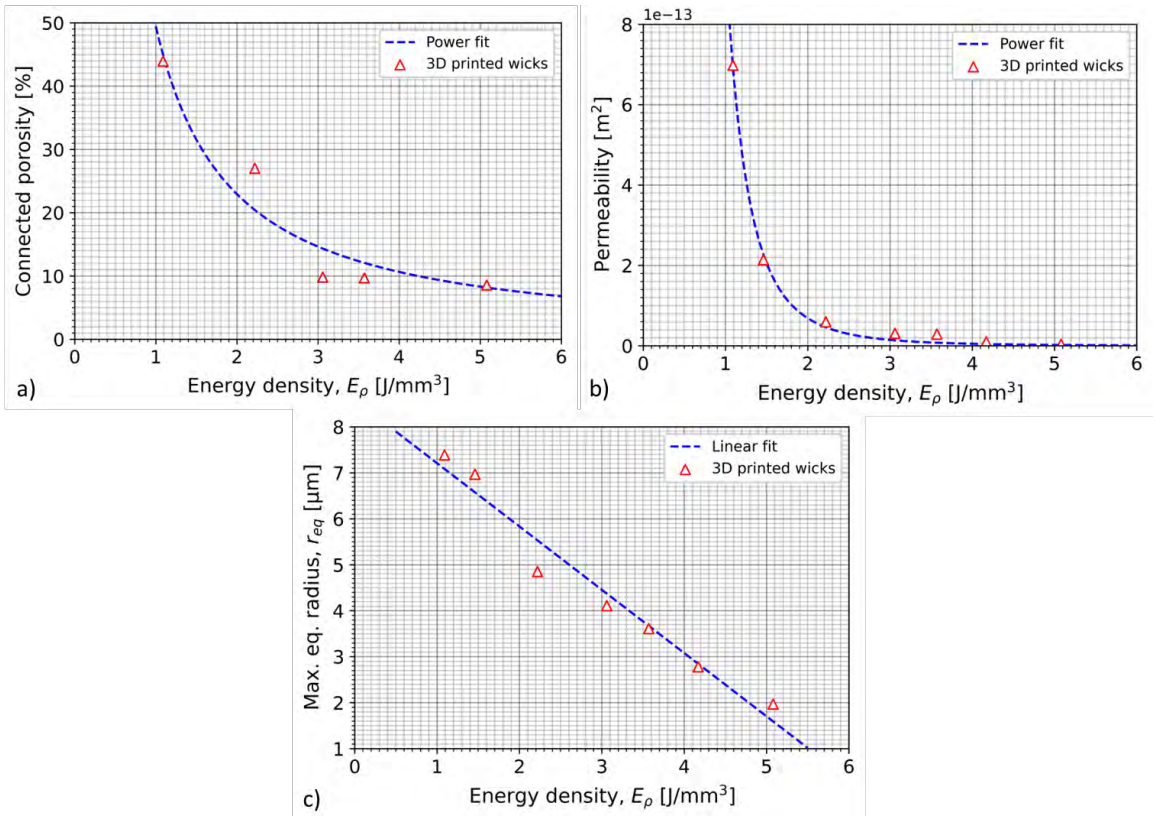

Figure 3. a) Connected porosity, b) permeability, and c) maximum equivalent pore radius of the successful 3D printed wick samples. Blue-dashed lines represent least-square fits.

Figure 4 shows a direct plot of the permeability and the maximum equivalent pore radius on a log-log scale for better clarity. The permeabilities are clearly seen to span a range of values greater than 10^{-15} m^2, as had been mentioned before.

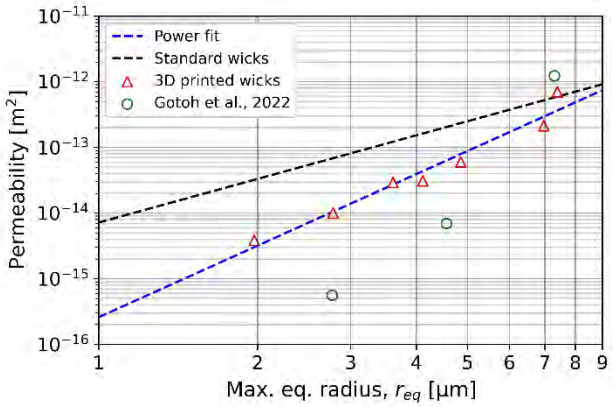

Figure 4. Maximum equivalent pore radius and permeability of the 3D printed wick samples. Green markers correspond to the 3D printed 316L SS wicks developed by Gotoh et al.[4] Blue-dashed line represents a least-squares fit through the current data while the black-dashed line is the corresponding fit through ACT's furnace-sintered wicks.

The blue-dashed line in Figure 4 corresponds to a least-squares power fit through the 3D printed samples. The black-dashed line is the corresponding fit through the standard, furnace-sintered wicks that have been manufactured over the years at ACT. Individual standard wicks are not shown in Figure 4 to preserve clarity. The 3D printed wick line shows a steeper decline in permeability with decreasing maximum pore radius than the standard wick line. However,

it should be emphasized that the standard wicks show significant variability about their corresponding fit, with some standard wicks having comparable permeabilities as the 3D printed wicks even at the smaller pore radii. The green markers in Figure 4 correspond to the 3D printed 316L SS wicks developed by Gotoh et al.[4] These samples show a steeper decline in permeability than the 3D printed wicks from the current study.

B. Mercury Intrusion Porosimetry

An interesting feature of the pore distribution in the 3D printed wicks is discussed in this section. Three specific wick samples, labelled as points 1, 2, and 3 in Figure 5, are selected for this discussion. The cumulative intrusion curves for points 1, 2, and 3 are presented in Figure 6.

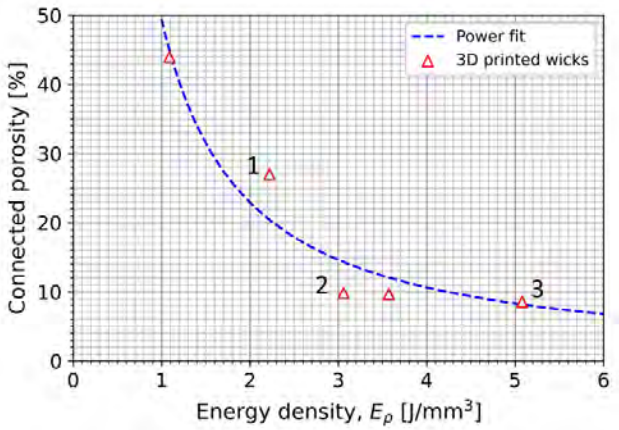

Figure 5. Porosity and energy density of the 3D printed wick samples. Points 1, 2, and 3 highlight the wicks selected for comparison.

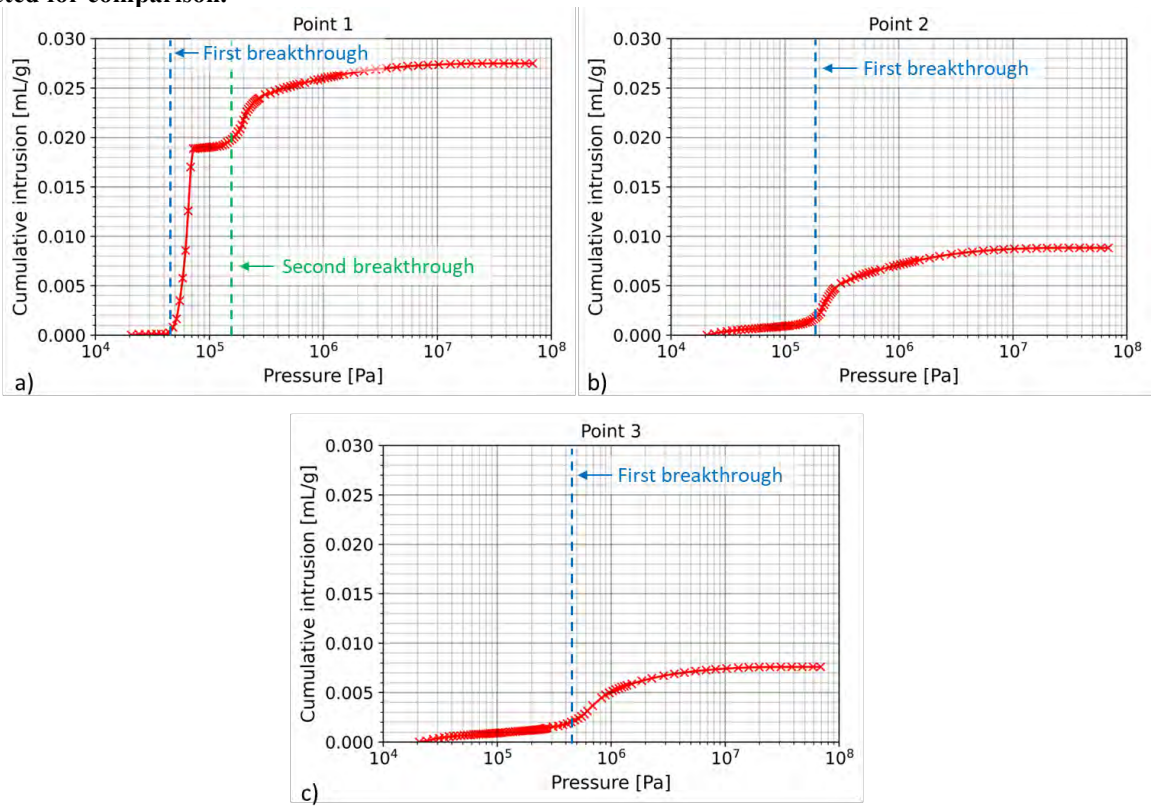

Figure 6. Cumulative intrusion curves from MIP for a) point 1, b) point 2, and c) point 3 wicks from Figure 5. Dashed vertical lines indicate approximate breakthrough pressures.

The approximate breakthrough points for each intrusion, characterized by a rapid percolation of mercury once the applied pressure crosses a minimum threshold, is highlighted in Figure 6. From Figure 6, the cumulative intrusion curve for point 1 is characterized by two distinct intrusion regions – an initial rapid intrusion past a low breakthrough pressure followed by a second intrusion past a much higher breakthrough pressure. The two intrusion regions are separated by a distinct intermittent plateau. This dual intrusion is also seen in the lower energy density sample lying to the left of point 1 in Figure 5. In the literature,[7,8] dual intrusion regions are seen in composite porous samples containing many separate porous regions. The initial breakthrough is associated with the filling of mercury in the interstitial voids between two distinct porous regions whereas the second breakthrough corresponds to the classic intrusion of mercury within each porous region. The low-pressure intrusion is, however, suppressed in the wick samples beyond E_ρ = 3 J/mm^3. These high-energy-density samples are associated with just a single intrusion region. For the point 1 wick sample, the dual intrusion regions are further investigated by splitting the cumulative intrusion curve at the blue-dashed line in Figure 7. The pressure at the blue-dashed line in Figure 7 corresponds to a Washburn pore radius of 5 µm. The intrusion curve thus divided is presented in Figure 8 as a function of the pore radius. The starting value for the second intrusion region is also reset to zero for ease of comparison. From the respective maximum intrusion values in Figure 8, the first intrusion region accounts for approximately 70% of the total connected porosity of the point 1 wick.

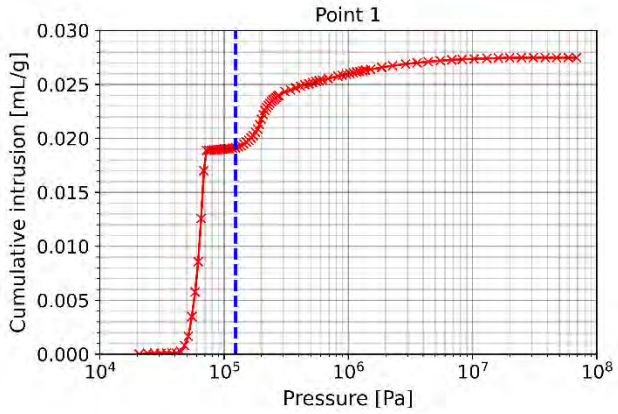

Figure 7. Cumulative intrusion curve from MIP for point 1 wick from Figure 5. Blue dashed line corresponds to the pressure at which the Washburn pore radius is 5 µm.

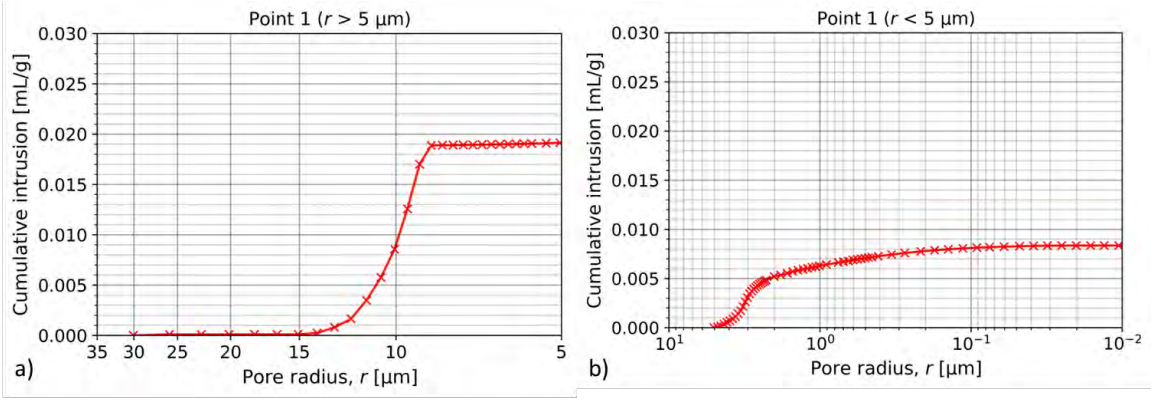

Figure 8. Cumulative intrusion curve for point 1 a) above a pore radius of 5 µm and b) below a pore radius of 5 µm with the starting intrusion value reset to zero.

Using the Katz-Thompson (K-T) relation presented in Equation 2, the permeability associated with the first intrusion region was determined to be over an order-of-magnitude greater than the measured permeability of 5.98 × 10^{-14} m^2 for the sample. In contrast, the second intrusion region accounting for just 30% of the connected porosity has a K-T permeability of 2.02 × 10^{-14} m^2, which is significantly closer to the measured value. As such, it is conjectured that the first intrusion region in the low-energy-density 3D printed wicks consists largely of dead-end pores that offer little contribution to the overall permeability despite accounting for a major fraction of the porosity. Any significant

contribution to the permeability from the first intrusion region would lead to an inexplicable discrepancy between the K-T and measured values. However, additional investigation with X-ray imaging is required to establish the presence of these dead-end pores with certainty. The cumulative intrusion curves for points 2 and 3 were also separated at a pore radius of 5 µm. Figure 9 shows a comparison of the three cumulative intrusion curves up to a pore radius of 5 µm. The starting intrusion value for each of the curves is reset to zero. The second intrusion region of the point 1 wick appears to align well with the trend established by points 2 and 3. The K-T permeabilities for the intrusion curves in Figure 9 are listed in Table 1. The general consistency between the K-T and measured permeabilities act to reinforce the conjecture that the through pores in the current low-energy-density wicks are primarily contained within the second intrusion region. In particular, the relative increase in permeability by a factor of eight from point 3 to point 2 and by a factor of two from point 2 to point 1 is accounted for almost entirely by the pores with radii under 5 µm. While the porosity gains at the lower energy densities are not majorly reflected in the permeability, the larger dead-end pores are still expected to improve the LHP thermal conductance by suppressing the heat leak through the wick.

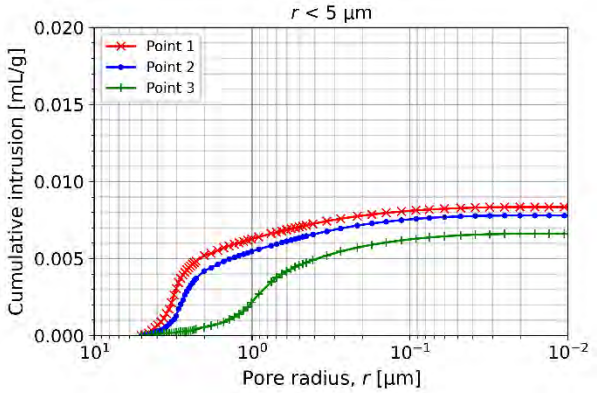

Figure 9. Comparison of the cumulative intrusion curves for points 1, 2, and 3 up to a pore radius of 5 µm. Note that the starting intrusion values for each curve has been reset to zero.

Table 1. Comparison of the K-T and measured permeabilities

Sample	K-T Permeability [in m^2]	Measured Permeability [in m^2]
Point 1	2.02×10^{-14}	5.98×10^{-14}
Point 2	1.07×10^{-14}	3.09×10^{-14}
Point 3	1.27×10^{-15}	3.85×10^{-15}

IV. Conclusion

The development of 3D printed wicks for LHPs by ACT is detailed in this paper. A custom composite variable, called the energy density, was defined combining the major build parameters associated with laser powder bed fusion. The energy density was then controlled to produce an assortment of wicks with varying capillary performance. Measurements of the capillary performance were acquired using a combination of capillary flow porometry and MIP. The connected porosity and permeability were found to decrease non-linearly with increasing energy density. The maximum equivalent pore radius, in contrast, was observed to decrease linearly with increasing energy density. As a highlight, a high-energy-density wick with a pore radius of under 2 µm and permeability of over 10^{-15} m^2 was successfully developed. The cumulative intrusion curves from MIP were studied to understand the pore distribution in the wicks. The low-energy-density wicks were associated with two distinct intrusion regions – a rapid low-pressure intrusion followed by a gradual high-pressure intrusion. The initial, low-pressure intrusion was found to be largely absent in the higher-energy-density wicks. The Katz-Thompson permeabilities from just the high-pressure intrusions were found to compare favorably with the measured permeabilities, indicating that the low-pressure intrusion occurred primarily in dead-end pores. Additional investigation with X-ray scanning is warranted to establish the morphology of pores with certainty. However, the results from the current study can serve as general guideline for future development of 3D printed wicks with the desired capillary metrics.

Acknowledgments

This work is funded by NASA through the Small Business Innovation Research (SBIR) program under contract 80NSSC21C0563. The technical monitor is Ms. Stephanie Mauro. The authors are grateful to Adam Shreve for performing the capillary flow measurements reported in this paper.

References

[1] Gupta, R., Chen, C-H., and Anderson, W.G., "Progress on 3D Printed Loop Heat Pipes," *50th International Conference on Environmental Systems*, 2021.
[2] Gupta, R., Chen, C-H., and Anderson, W.G., "Experiments on a Loop Heat Pipe with a 3D Printed Evaporator," *51st International Conference on Environmental Systems*, 2022.
[3] Mezghani, A., Nassar, A.R., Dickman, C.J., Valdes, E., and Alvarado, R., "Laser Powder Bed Fusion Additive Manufacturing of Copper Wicking Structures: Fabrication and Capillary Characterization," *Rapid Prototyping Journal*, Vol. 27, No. 6, 2021, pp. 1181-1188.
[4] Gotoh, R., Furst, B.I., Roberts, S.N., Cappucci, S., Daimaru, T., and Sunada, E.T., "Experimental and Analytical Investigations of AlSi10Mg, Stainless Steel, Inconel 625 and Ti-6Al-4V Porous Materials Printed via Powder Bed Fusion," *Progress in Additive Manufacturing*, Vol. 7, No. 5, 2022, pp. 943-955.
[5] Katz, A.J. and Thompson, A.H., "Quantitative Prediction of Permeability in Porous Rock," *Physical Review B*, Vol. 34, No. 11, 1986, pp. 8179.
[6] Katz, A.J. and Thompson, A.H., "Prediction of Rock Electrical Conductivity from Mercury Injection Measurements," *Journal of Geophysical Research: Solid Earth*, Vol. 92, No. B1, 1987, pp. 599-607.
[7] Webb, P.A. and Orr, C., "Analytical Methods in Fine Particle Technology," Micromeritics Instrument Corporation, 1997.
[8] Rouquerol, J., Baron, G., Denoyel, R., Giesche, H., Groen, J., Klobes, P., Levitz, P., Neimark, A.V., Rigby, S., Skudas, R., and Sing, K., "Liquid Intrusion and Alternative Methods for the Characterization of Macroporous Materials (IUPAC Technical Report)," *Pure and Applied Chemistry*, Vol. 84, No. 1, 2011, pp. 107-136.